University of Bath

Influence of Flow Coefficient on Ingress Through Turbine Rim Seals

Dimitrios Graikos, Mauro Carnevale, Carl M Sangan, Gary D Lock and James A Scobie
dg698@bath.ac.uk, mc2497@bath.ac.uk, c.m.sangan@bath.ac.uk,
g.d.lock@bath.ac.uk and j.a.scobie@bath.ac.uk
Department of Mechanical Engineering
University of Bath
Bath, BA2 7AY
United Kingdom

ABSTRACT

Rim seals are critical in terms of limiting the temperature of highly-stressed engine components but function with a penalty to the power output and contribute to entropy gain stemming from mixing losses in the turbine. Ingress through rim seals is influenced by the presence of rotor blades and stator vanes, and the mainstream flow coefficient in the annulus that determines the corresponding swirl.

This paper presents an experimental study of ingress upstream and downstream of the rotor disc in a 1.5-stage rig with double radial clearance rim seals. Two rotor discs were used, one with blades and one without, and two platforms were used downstream of the rotor, one with vanes and one without. Tests were conducted at two rotational speeds and a range of flow conditions was achieved by varying the annulus and sealing mass flow rates. Concentration effectiveness, swirl and steady pressure measurements separated, for the first time, the influence of the blades and vanes on ingress over a wide range of flow conditions. Measurements on the downstream stator platform provide added insight into the complex interaction between the egress and the mainstream. Measurements of unsteady pressure revealed the presence of large-scale structures, even in the absence of blades. The number and speed of the structures was shown to depend on the flow coefficient and the purge flow rate.

1 INTRODUCTION

High-efficiency operation of industrial gas turbines and aircraft engines are critical in the required reduction of carbon dioxide emissions to mitigate the change in global climate [1]. The most advanced combined cycle plants (known as H class) reach efficiencies in excess of 60%. Here the turbine entry temperature exceeds the melting point of metal components. To maintain integrity, high-pressure air is extracted from the compressor and distributed throughout the engine through the secondary air system for cooling and sealing purposes. Superfluous use of secondary air reduces engine efficiency and performance, while insufficient use can be detrimental to the life of vulnerable components operating at the extreme limits of thermal and mechanical stress.

A key function of the secondary air system is to pressurise the wheel-space formed between the rotating and stationary turbine discs in order to minimise the ingress (ingestion) of hot gases from the mainstream annulus. Rim seals are fitted at the periphery of the discs to reduce the volume of sealing flow (or purge) required to supress ingress to acceptable levels. Careful design is required to minimise mixing losses of egress through the rim seal with the mainstream flow. Expensive full-scale engine tests are used to determine the minimum level of purge to limit metal temperatures. To reduce testing, designers require reliable predictive methods and experimental data from rigs simulating the engine.

Figure 1 shows a typical turbine stage with a wheel-space upstream and downstream of the rotor. Previous research has identified three primary mechanisms governing ingress: *rotationally-induced* effects associated with entrainment and disc pumping; *externally-induced* effects driven by the pressure asymmetry in the annulus; and *unsteady* effects manifested by large-scale structures rotating below the blade-passing

frequency near the rim-seal. These primary mechanisms are influenced by the stage geometry (vanes, blades and rim seal) and, in non-dimensional form, the purge, disc rotational Reynolds number and flow coefficient in the mainstream annulus.

This paper describes an experimental study using an engine-representative turbine stage that simulates ingress into wheel-spaces upstream and downstream of the rotor disc. A generic double radial-clearance rim seal was used as part of this study. Experimental data were collected over a range of mainstream annulus flow coefficient, which influenced the vane and blade pressure fields. Two rotor discs were used, one with blades and one without (cylindrical rotor); two platforms were used downstream of the rotor, one with vanes and one without (cylindrical ring). The experiments were conducted at two rotational Reynolds numbers and the purge flow rates were varied to create a large range of test conditions. The aim of this study was to characterise the effect of the aerodynamic profile downstream of the rim seal (i.e. the blade for the upstream wheel-space and the downstream vane for the downstream wheel-space) over a wide range of flow coefficient.
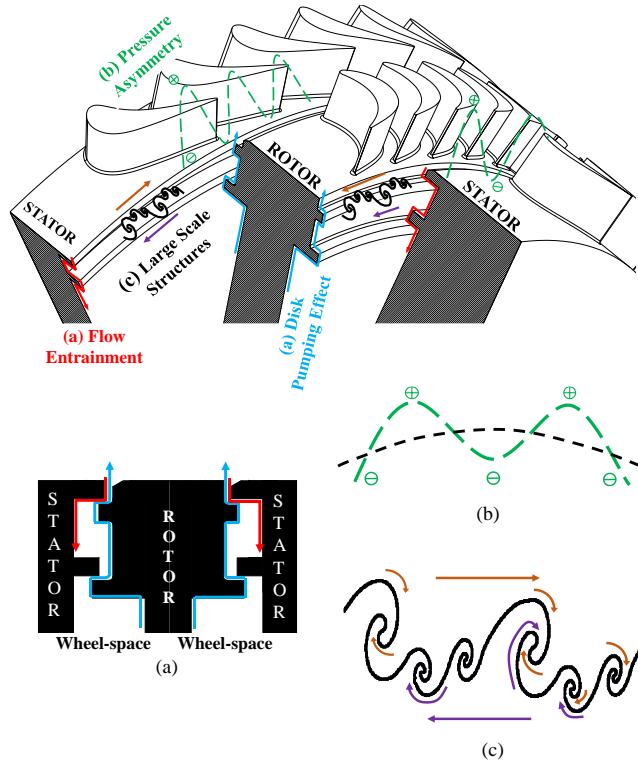
Figure 1: Typical axial turbine stage depicting the principal flow mechanisms governing ingress

2 LITERATURE REVIEW

For extensive reviews on the topic of ingress, the reader is directed towards Scobie *et al.* [2] and Chew *et al.* [3]. Rim seals feature at the periphery of the wheel-space with ingress and egress from/to an annulus flow with high swirl and non-axisymmetric pressure field created by stationary vanes and rotating blades; this is illustrated in Figure 1. Early studies focussed on *rotationally-induced* (RI) effects without mainstream flow, showing ingress depended on the purge mass flow, seal geometry and the rotational Reynolds number. Later studies with engine-representative mainstream flow showed the importance and dominance of pressure asymmetry governing *externally-induced* ingress; here the circumferential asymmetry creates unsteady pockets of ingress and egress through the seal clearance. In recent studies, unsteady computational fluid

dynamics has revealed large scale instabilities that rotate at a fraction of the disc speed. The presence of these structures has subsequently been confirmed by experimental data and shown to influence the level of ingress. There is an unsteady interaction between the egress of purge and the main annulus flow that has an impact on the radial migration of the secondary flow and aerodynamics losses. Interest from engine designers on this topic continues and the review below will concentrate on the most recent developments.

Revert *et al.* [4] reported the sealing performance of a chute seal under RI conditions using a rotor disc without blades, and axisymmetric and non-axisymmetric annulus flow. A range of flow coefficients were achieved by keeping the mainstream flow constant and varying the rotational speed of the disc. The sealing effectiveness inside the wheel-space reduced for increased rotor speeds at constant purge flow rate under axisymmetric conditions. The inverse phenomenon was observed when the stator vanes were introduced. Hualca *et al.* [5] made measurements of sealing effectiveness for two upstream vanes positions relative to the rim seal. Curves of effectiveness as a function of non-dimensional purge were broadly unaffected by the steady levels of pressure asymmetry in the annulus. The effect of the rotor blades was isolated using a bladed and bladeless disc; there was a clear influence of the blade, depending on the level of purge.

Beard *et al.* [6] experimentally identified unsteady large-scale structures using a single-stage rig with no vanes and blades, and in the absence of a mainstream anulus flow. Fast response pressure transducers were installed at various circumferential and radial positions near and inside the rim seal. The results showed that the level of unsteadiness inside the seal gap was higher than that in the cavity, with a broader spread of frequencies. Inside the wheel-space, 26-29 structures were identified rotating at approximately 80% of the disc speed. Hualca *et al.* [5], as have others, have shown

these structures have a distinct frequency different to that of the rotating blades with annulus flow; however, these instabilities were influenced by the presence/absence of blades. Savov *et al.* [7] measured unsteady pressures for two seals, with and without rotor blades. Increased activity was observed for the bladeless case. The authors associated the formation of the structures to Kelvin-Helmholtz instabilities.

Several computational studies have investigated the rotational frequency and structure of these instabilities, and physically link them to their causal phenomenon. Horwood *et al.* [8] showed the number of instabilities and their rotational frequency relative to the disc was influenced by the purge flow rate. Postulated driving mechanisms for these structures include Kelvin-Helmholtz and Taylor-Couette instabilities; Gao *et al.* [9] show the fundamental mechanism for this phenomenon may be understood in terms of inertial waves.

Gallier *et al.* [10] used particle-image-velocimetry to investigate the interaction between egress and the annulus flow at the hub approaching the rotor blades. The blades were shown to increase the momentum of the fluid at the hub, allowing the cold purge air to remain attached to the rotor platform until it impinged at the leading edge. Schädler *et al.* [11] experimentally investigated the rim-seal exit using fast-response aerodynamic probes, showing the flow field is strongly influenced by the amount of ejected purge. Specifically, clear turbine hub cavity modes were identified and linked to an aerodynamic loss mechanism.

3 EXPERIMENTAL FACILITY

The University of Bath 1.5-stage axial turbine rig experimentally models ingress upstream and downstream of the rotor disc. The rig operated under fluid-dynamically-scaled conditions at a rotational Reynolds number $\sim 10^6$. The versatility of the rig offers

close monitoring of the factors that affect ingress. A comprehensive description of the facility is provided by Patinios *et al.* [12]. Since Hualca *et al.* [5], the rotor blades and downstream vanes have been re-designed to increase the stage reaction. The rig accommodates a modular process where blades, bliscs, blings and vanes can be removed or introduced.

Mainstream annulus flow is supplied to the rig by a 160 kW Atlas Copco compressor capable of delivering flow up to 1.5 kg/s at a pressure of 1.2 bar gauge. The flow was regulated by altering the load of the compressor and measured using a thermal mass flow meter. A heat exchanger ensured that the flow temperature was $(20 \pm 2)°C$ before reaching an annular transition that ensured axisymmetry upstream of the vanes. In full configuration, the test section features an upstream stator with 32 vanes, a rotor with 48 turned blades and a downstream stator with 32 vanes; all the aerodynamic profiles are prismatic (2D). The diameter of the stator disc was 380 mm. As part of a flexible design, the vanes were manufactured as modular bladed rings (blings). The rotor was machined from a single piece of titanium as a bladed disc (blisc). The blisc was rotated up to 6000 rpm by a 34 kW dynamometer, which could also absorb any generated power. The blisc and blings could be substituted to versions without blades or vanes, depending on the experimental requirements.
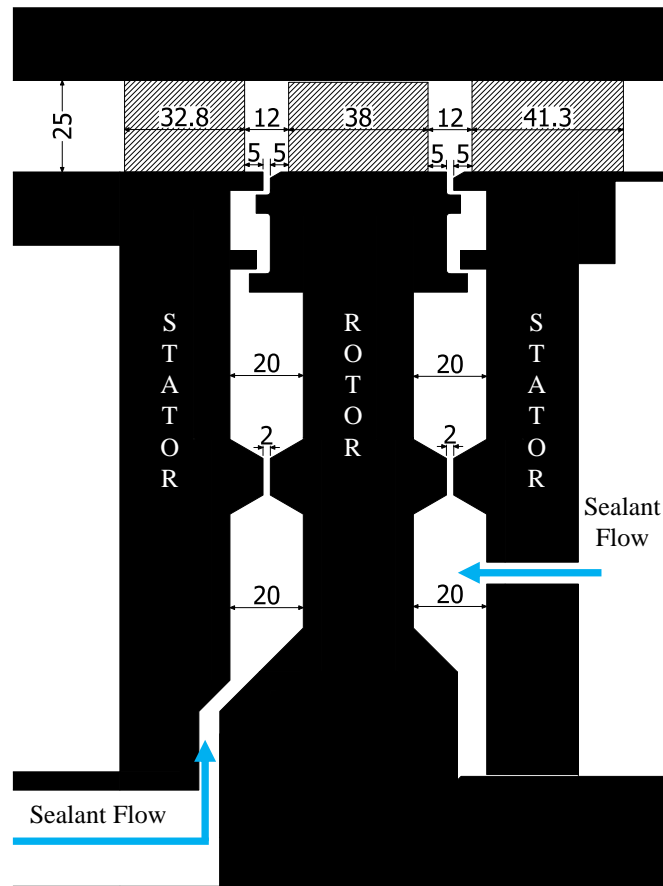
Figure 2: Cross section of rig showing sealing flow supply to upstream and downstream wheel-spaces

Sealing flow (purge) was introduced in the upstream and downstream wheel-spaces independently at a low radius, as shown in Figure 2. In both cases an inlet seal ensured that the flow entering the main cavity was axisymmetric and well-conditioned. A thermal mass flow meter (accuracy of $\pm1\%$ of their full-scale range), coupled with control valves, was used to regulate and measure the flow. The sealing flow rate is expressed in non-dimensional form as Φ_0, which is an inviscid parameter that takes into account the rotational speed; Φ_0 equates to the bulk mean radial seal velocity normalised by the disc speed.

$$\Phi_0 = \frac{C_{w,0}}{2\pi G_c Re_\phi} = \frac{U}{\Omega\, b} \tag{1}$$

All symbols are defined in the nomenclature.

3.1 Operating Conditions

The range of operating conditions is summarised in Table 1. A range of flow coefficients was achieved by keeping the rotor speed constant and varying the annulus mass flow rate.

Parameters	Disc Speed (rpm)	
	3000	4000
Rotational Reynolds Number, Re_ϕ	7.4×10^5	1.0×10^6
Axial Reynolds Number, Re_w	$(1.9-3.7) \times 10^5$	$(2.6-4.4) \times 10^5$
Flow Coefficient, C_F	$0.26-0.5$	$0.26-0.44$
Vane exit Mach Number, M	$0.20-0.38$	$0.24-0.45$

Table 1: Operating conditions

3.2 Gas Concentration Measurements

Levels of ingress from the annulus inside the wheel-space were measured using a gas concentration technique. The sealing flow was seeded with a tracer gas, $0.5-1\%$ CO_2. The sealing effectiveness (ε_c) is defined as follows:

$$\varepsilon_c = \frac{c - c_a}{c_0 - c_a} \qquad (2)$$

where c is the measured concentration and the subscripts a and 0 denote the values measured in the annulus and in the sealing flow at the inlet of the wheel-space respectively. Both c_a and c_0 are sampled using single point tapings on the surface of the annulus and the sealing flow lines respectively. In both cases, fully mixed out measurements are ensured. The annulus flow had an inherent concentration, $c_a \approx$ 0.045% - equivalent to atmospheric levels of CO_2 in air. The annulus flow had an inherent concentration, $c_a \approx 0.045\%$.

The radial distribution of concentration on the stator and in the rotating core of both upstream and downstream wheel-spaces was measured using sampling taps as shown in Figure 3. The concentration on the vane platform downstream of the rotor was measured using 15 taps that extended over a vane pitch (11.25°).

The concentration of CO_2 was measured using a Signal Group 9000MGA multi-gas analyser and a 20-channel multiplexer. The multiplexer consists of solenoid valves, which can be triggered to sample flow from up to 20 different locations, one at a time. The gas analyser had an accuracy, repeatability and linearity of ±0.5% of its full-scale range. The gas sampled from the measurement location was analysed for at least 30 s before its concentration value stabilised, and then averaged over 10 s.
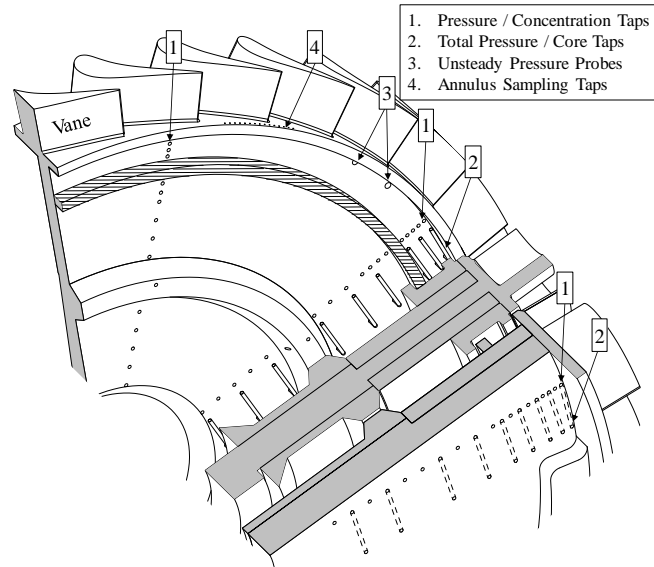
Figure 3: Test section and instrumentation

3.3 Pressure Measurements

Four Scani-valves, with 48 channels, allowed pressures to be measured with the same differential transducer, reducing uncertainty. The pressure was sampled and averaged over 2 s at each measurement location.

The steady pressure variation across the upstream vane pitch in the annulus was measured on the stator hub 2.5 mm downstream of the trailing edge of vane. The circumferential pressure variation downstream of the rotor was measured on the stator hub 2.5mm upstream the leading edge of vane. A vane pitch spanned 11.25˚ and the circumferential distribution of pressure was measured using 15 taps. The data is presented below using a non-dimensional pressure coefficient $C_{p,a}$ - see nomenclature.

Static pressure was collected in the wheel-space from the same radial distribution of taps used for the concentration measurements. The tangential component of velocity, and hence the swirl inside the inviscid core, was determined from total pressure was measured at $z/S = 0.25$ using pitot probes.

Two Kulite XCS-062 differential pressure transducers collected the unsteady pressure in the upstream wheel-space. At 3000 rpm, the blade passing frequency (BPF) is 2.4 kHz, which is significantly lower than the natural frequency of the transducer (150 kHz). The sensors were flush mounted on the stator wall and installed below the stator lip at a radius $r/b = 0.993$, circumferentially displaced by an angle $\alpha = 8°$. Data was sampled over 10 s at 100 kHz (equivalent to 500 disk revolutions), resulting into two signals with a phase difference. A 50 kHz low-pass filter was fitted upstream of the data-acquisition system to prevent aliasing. The two signals were analysed as fast Fourier transforms (FFTs) of windowed segments of the signals and cross-correlated to determine the angular speed and number of structures (see [6] for more details). A rectangular window was used to obtain frequency resolution and reduced spectral leakage. The spectral analysis of the data is presented as a non-dimensional unsteady pressure coefficient C_p, which is defined in the nomenclature.

3.4 Double Radial Clearance Seal

A generic double radial clearance seal was used in both wheel-spaces. Figure 4 and Table 2 show the main characteristics of the seal geometry. The seal divides the main wheel-space into two cavities. Intense mixing between the purge and ingress occurs in the buffer or outer cavity. Here the external influence of the annulus and associated unsteady phenomena is most acute. In the engine, this would be expected to be the hottest and most vulnerable part of the wheel-space. Less ingress will penetrate to the inner cavity where rotational effects may dominate.
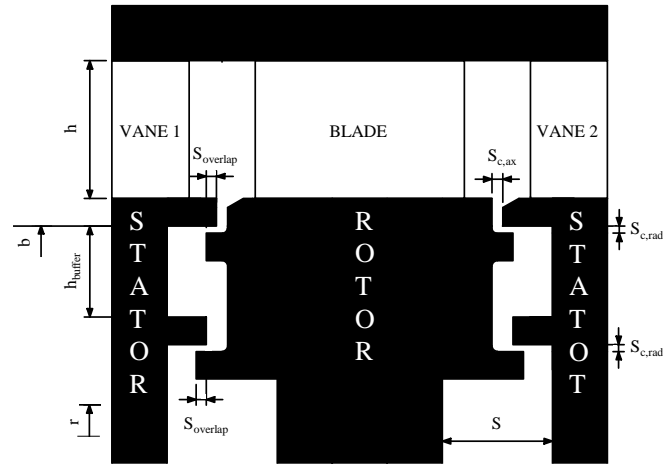
Figure 4: Double radial seal configuration in the upstream and downstream wheel-spaces

Parameter	Dimension (mm)
h	25
b	190
S	20
h_{buffer}	16.5
$s_{c,ax}$	2
$s_{overlap}$	1.86
$s_{c,rad}$	1.28

Table 2: Geometric parameters

4 RESULTS

This section presents experimental measurements in both the upstream and downstream wheel-spaces. The four configurations tested are presented in Figure 5.

Configurations (c) and (d) have the advantage of static instrumentation downstream of the rim seal clearance, presenting the opportunity for measurements of the emerging egress. As shown in this section, the influence of the downstream aerodynamic profile on ingress in both the upstream and downstream wheel-space is similar. Insight gained from the measurements in the downstream side can therefore be applied in the context of the upstream wheel-space, and *vice versa*.

(a)   (b)

(c)   (d)
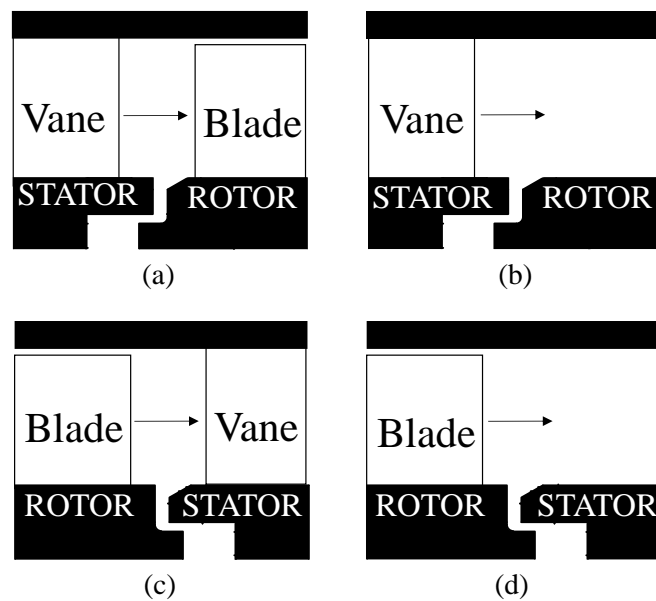
Figure 5: Four configurations tested, upstream - (a) and (b) and downstream –

(c) and (d)

4.1 Upstream Wheel-Space

Figure 6 shows the radial variation of concentration effectiveness ε_c in the upstream wheel-space. Data has been collected with and without the rotor blades. The effectiveness was measured on the stator wall at 15 radial locations as shown in the silhouette. The external flow direction was from left to right with axial Reynolds number $Re_w = 2.6 \times 10^5$ and rotational Reynolds number $Re_\phi = 7.4 \times 10^5$, resulting in a

flow coefficient $C_F = 0.35$. Three different purge flow rates (Φ_0) were tested for both cases resulting in six distributions.

Outer Cavity 1: At high radius the effectiveness increases rapidly across the rim seal from $\varepsilon_c = 0$ in the annulus as the ingested fluid is mixed with the sealing flow. Externally-induced (EI) ingress and unsteady phenomena dominate here. Ingress is suppressed as the purge increases and the wheel-space is pressurised. There is a significant influence of the rotor blades, which increase the level of ingress, except at high purge where this outer cavity is almost sealed. The effectiveness is virtually invariant with radius, indicating the stator boundary layer is fully mixed immediately inboard of the rim seal. Though not shown here, the data was independent of Re_ϕ at constant C_F.

Inner Cavity 2: Some of the mixed fluid from the outer cavity penetrates to the inner cavity and is further mixed with the purge flow. The blades still affect ingress but the influence is diminished. It is expected that rotationally-induced effects, rather than EI effects are dominant across the inner rim seal.

*Purge Inlet Region 3*: Here the effectiveness is unity, with no ingress.
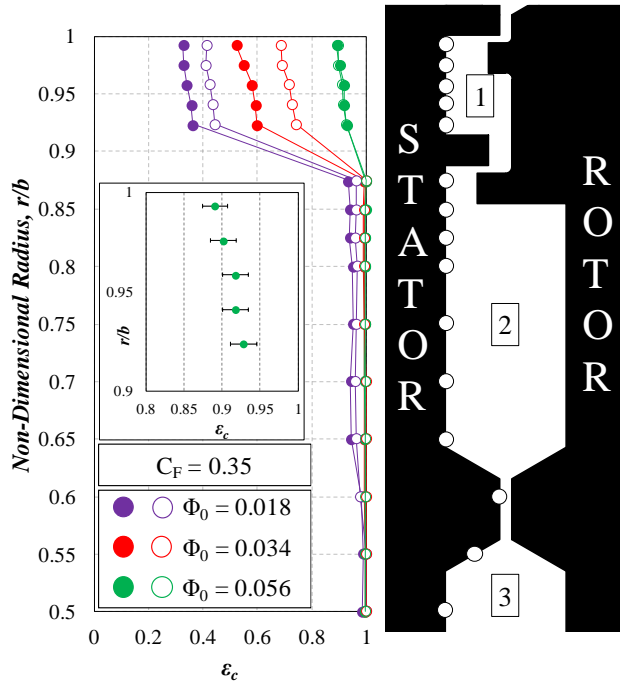
Figure 6: Radial distribution of effectiveness in the upstream wheel-space. (Re_ϕ = 7.4×10^5) (open symbols: bladeless rotor; solid symbols: bladed rotor).

Figure 7 shows the variation of concentration effectiveness (ε_c) with flow coefficient (C_F) for three levels of non-dimensional purge (Φ_0). Effectiveness was measured at r/b = 0.958 in the outer cavity, where the concentration does not vary significantly with radius. The data was collected at constant purge flow rate and rotational speed; the mainstream annulus flow rate was varied, providing a range of flow coefficients. The procedure was then repeated for the second rotational speed and the results are shown to be Re_ϕ independent over the range tested.

Experiments were conducted with and without rotor blades, with data marked by the closed and open symbols respectively – see also the silhouette for further clarity. When the blades are not present, ε_c reduces monotonically with increasing C_F and increasing swirl in the annulus. Increasing Φ_0 increases ε_c as expected. Generally, the blades increase ingress with the data following a similar characteristic curve. However, the

blades create a marked effect over a relatively narrow range of C_F with the data departing from the monotonic characteristic. For example, for $\Phi_0 = 0.056$ the blades create a significant increase in ingress relative to the non-bladed configuration over the range $0.35 < C_F < 0.41$. This range corresponds to a sweep of relative flow angle (determined from the vane inviscid velocity triangle – see Appendix) equivalent to the leading edge of the blade, as shown in Figure 8. The variation in relative flow angle (β_2) with C_F is indicted on the secondary abscissa and marked on Figure 7.

The data suggests the pressure field created by the downstream blades augments ingestion through the rim seal into the upstream wheel-space. The phenomenon is independent of rotational Reynolds number. For increased purge momentum (*i.e.* larger Φ_0) the minima in effectiveness occurs at larger C_F. This suggests that the egress interacts with the mainstream and modifies the velocity triangle near the hub and the corresponding local flow coefficient. Note that Gallier *et al.* [10] experimentally showed impingement of egress with the leading edge of the downstream blade.
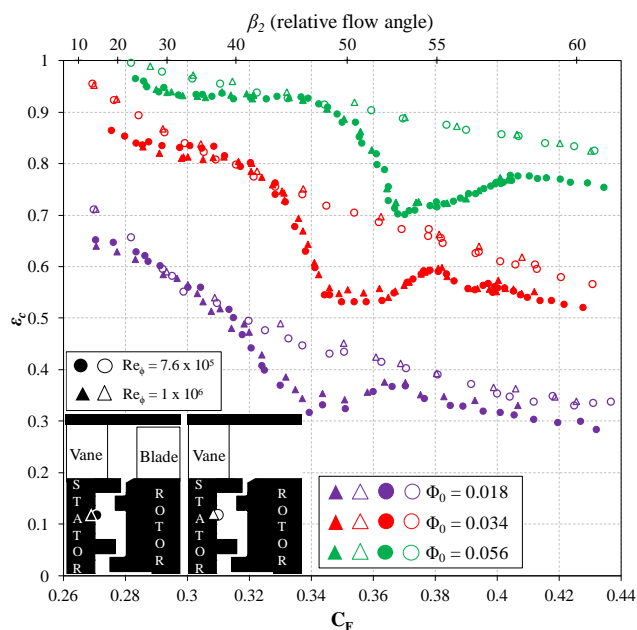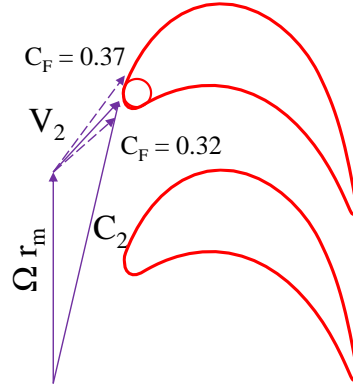
**Figure 8: Sweep of relative velocity vector across leading edge of the blade (Φ_0 = 0.018)**

Figure 9 (a) and (b) show the variation of ε_c against Φ_0 for the bladed and bladeless rotor at C_F = 0.35 and 0.407 respectively. Concentration was measured at two radial positions (r/b = 0.958 and 0.85) in the outer and inner cavities for two rotational speeds; the data is shown to be independent of rotational Reynolds number over the range tested. The three purge flow rates from Figure 7 are marked in colour.

Consider first the outer cavity and Figure 9 (a). Without blades the effectiveness curve follows a conventional shape without inflexions, similar to those described by Scobie *et al.* [2], with an increase in effectiveness as the purge pressurises the wheel-space. Ingress increases in the presence of blades with a marked effect over a narrow range of Φ_0 where the curve exhibits an inflexion. The inner cavity is protected by the second seal though influence of the blades is still apparent.

Figure 9 (b) shows similar trends though the inflexion of the effectiveness curve with blades occurs at a higher range of Φ_0; this is consistent with Figure 7, which shows that the impact of the blades is dependent on both C_F and Φ_0.
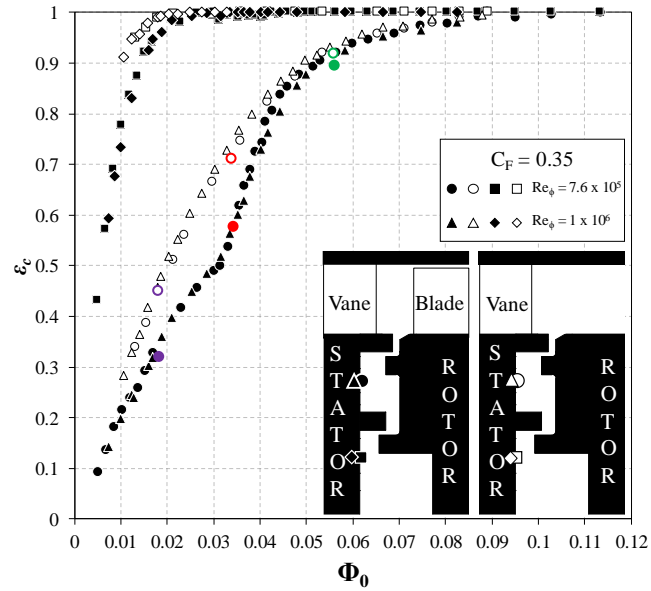

(a)
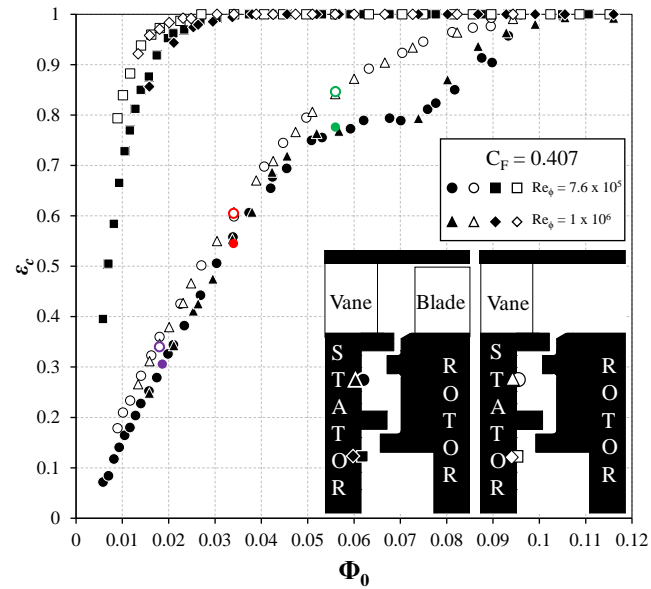
(b)

Figure 9: Sealing effectiveness against sealing flow rate at *r/b* = 0.958 (Circles and Triangles) and *r/b* = 0.85 (Squares and Diamonds). (a) C_F = 0.35, (b) C_F = 0.407. (Solid symbols: Rotor with blades), (Open symbols: Rotor without blades)

Figure 10 shows the variation of swirl ratio β in the upstream wheel-space against flow coefficient. The swirl was measured in the rotating core at $z/S = ¼$ and $r/b = 0.993$ with and without the rotor blades. The data was collected for two purge flow rates, both at the lower rotational speed ($Re_\phi = 7.6 \times 10^5$), with and without the blades. For both configurations the swirl ratio reduces with increased purge flow rate as the core rotation in the wheel-space is supressed. The annulus swirl ratio, β_a, increases linearly from 1.02 to 1.73 across the range of flow coefficients tested ($C_F = 0.26$ to $C_F = 0.44$). Without the blades, β increases monotonically with increasing C_F as the increasingly highly swirled flow enters the wheel-space. For all flow coefficients the blades increase the swirl ratio relative to the bladeless case, with a departure from the monotonic trend over a range consistent with Figure 7; here highly swirled fluid enters the outer cavity, demonstrating a clear link between ingestion and swirl. The maxima in swirl within this disturbed region aligns with the minima in effectiveness in Figure 7. For increased purge momentum (*i.e.* larger Φ_0) the maxima in swirl occurs at larger C_F, again suggesting the egress has an impact on the mainstream flow conditions.
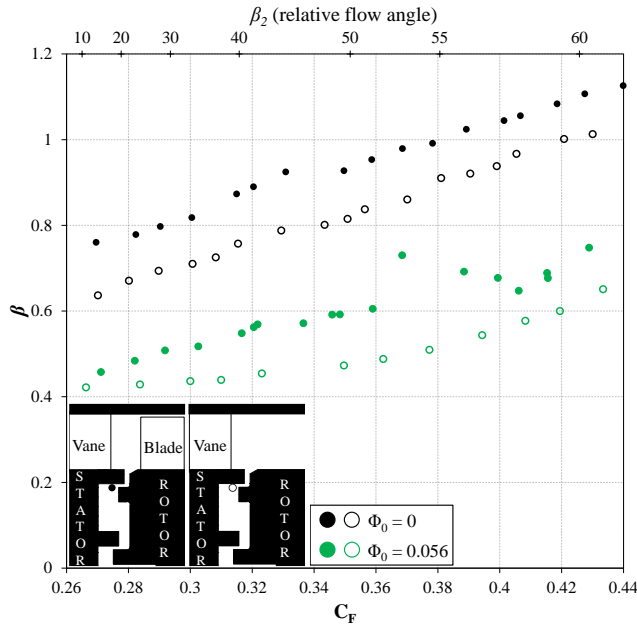
Figure 10: Variation of swirl ratio β with flow coefficient C_F at $r/b = 0.993$. (Solid symbols: Rotor with blades), (Open symbols: Rotor without blades), $Re_\phi = 7.6 \times 10^5$

Figure 11 shows the circumferential variation of steady pressure coefficient on the stator platform in the annulus over one vane pitch. The measurements are presented for the intermediate sealing flow rate ($\Phi_0 = 0.034$) and for three flow coefficients, with and without the rotor blades. Note that Patinios *et al.* [13] have shown $\Delta C_{p,a}^{1/2}$ upstream of the blades is proportional to C_F; this is consistent with the data collected here and the general reduction in effectiveness with C_F. Despite the increase in ingestion demonstrated in Figure 7, the influence of the blades has not been sensed in the pressure distribution upstream of the seal clearance.

It is hypothesised that if measurements on the rotating platform were possible, this influence would have been captured in the pressure distribution associated with the blade downstream of the clearance. The next section considers the downstream wheel-

space, where measurements of this kind are possible due to the downstream stationary surface.
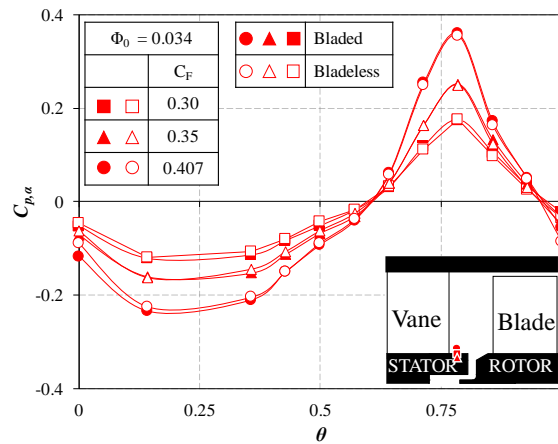

Figure 11: Variation of steady pressure coefficient in the annulus over a non-dimensional vane pitch ($\Phi_0 = 0.018$), $Re_\phi = 7.6 \times 10^5$

4.2 Downstream Wheel-Space

Figure 12 shows the radial variation of concentration effectiveness in the downstream wheel-space with and without the vanes further downstream. The points and discussion raised above with regards to Figure 6 and the upstream wheel-space apply equally here. The vanes downstream of the wheel-space have increased ingress in a similar manner to the blades in the upstream wheel-space. Note here the inner cavity is virtually sealed for the two larger purge flow rates. At common flow coefficient and purge flow rate there is less ingress in the downstream wheel-space in comparison to upstream. The two seals are geometrically a mirror image; however, the mainstream swirl differs in the two configurations and as the egress is pumped up the rotor, a fluid barrier may inhibit ingress downstream.
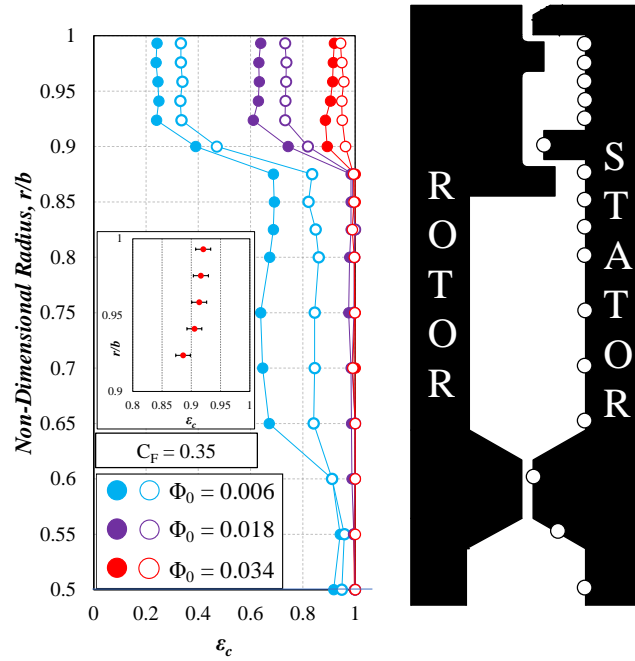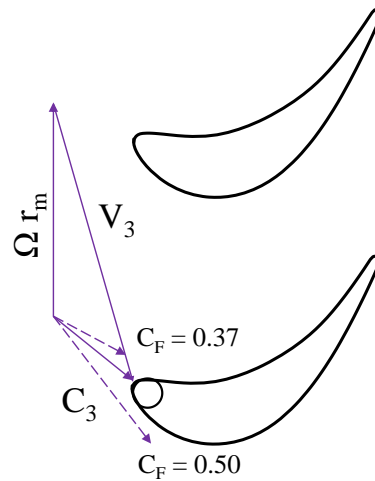
Figure 12: Radial distribution of effectiveness in the downstream wheel-space. ($Re_\phi = 7.4 \times 10^5$) (Solid symbols: Platform with vanes), (Open symbols: Platform without vanes).
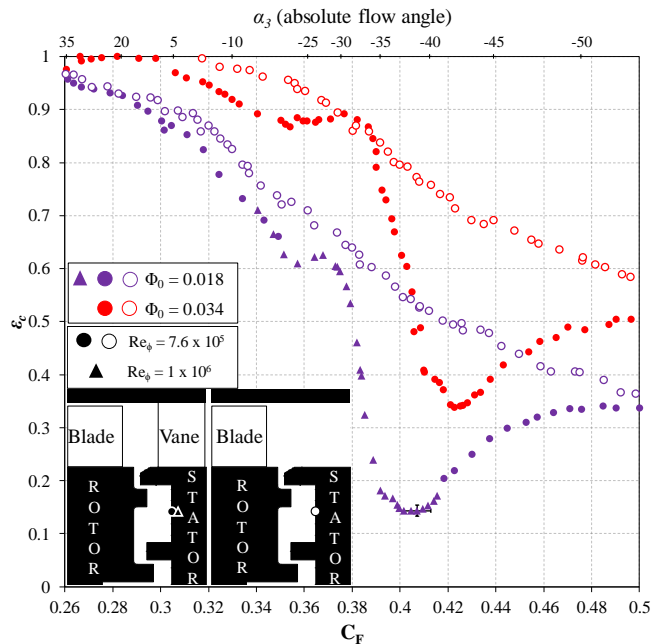
Figure 13: Effectiveness ε_c against flow coefficient C_F at $r/b = 0.958$. (Open symbols: Vaneless platform, Solid symbols: Platform with the vanes), $Re_\phi = 7 \times 10^5$

Figure 14: Sweep of absolute velocity vector across leading edge of the downstream vane ($\Phi_0 = 0.018$)
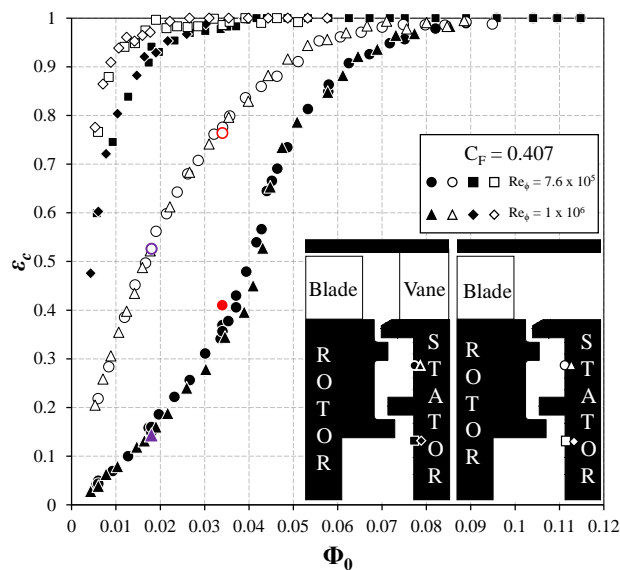
Figure 13 shows the variation of effectiveness with C_F measured in the outer cavity on the stator downstream of the rotor disc at $r/b = 0.958$. Analogous to the upstream data presented in Figure 7, two configurations were tested: platforms with and without vanes downstream of the rotor. The effectiveness measured using the vaneless platform decreases monotonically with C_F, following the same behaviour as the bladeless data upstream. Increasing the purge reduces ingress as the wheel-space is pressurised.

Generally, the vanes increase ingress with a marked effect over a relatively narrow range of C_F. As was the case upstream, this range corresponds to a sweep of absolute flow angle (determined from the vane inviscid velocity triangle – see Appendix) equivalent to the downstream vane leading edge. This is shown in Figure 14 for the range of flow coefficients corresponding to the dip at $\Phi_0 = 0.018$. For increased purge momentum (*i.e.* larger Φ_0) the minima in effectiveness occurs at larger C_F, suggesting an interaction between the egress and the mainstream. The effect of the vanes is strongest at the highest purge level tested.

Figure 15 (a) and (b) show the variation of ε_c against Φ_0 for the cases with and without the downstream vanes at $C_F = 0.35$ and 0.407 respectively. Concentration was measured at two radial positions ($r/b = 0.958$ and 0.85) in the outer and inner cavities where the vanes have increased ingress at all levels of purge. The three purge flow rates from Figure 13 are marked in colour. The differences in the curves in both the inner and outer cavities are more pronounced at the larger flow coefficient. Much of the discussion with reference to Figure 9 above is relevant here.


(a)
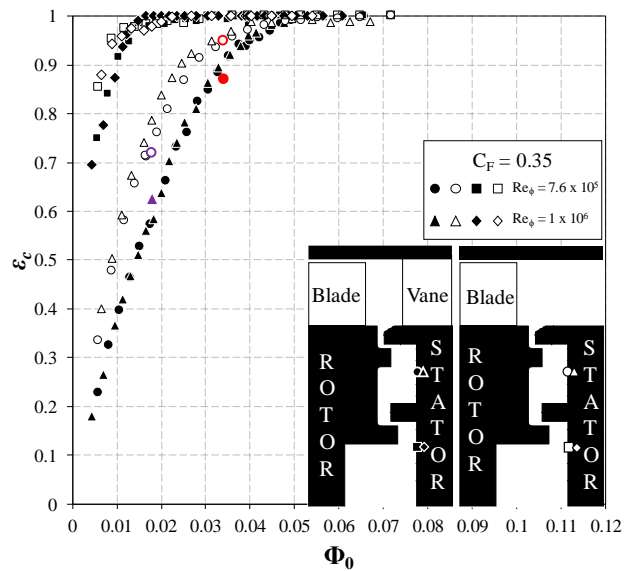
Figure 15: Sealing effectiveness against sealing flow rate at *r/b* = 0.958 (Circles and Triangles) and *r/b* = 0.85 (Squares and Diamonds). (a) C_F = 0.35, (b) C_F = 0.407. (Solid symbols: Platform with vanes), (Open symbols: Platform without vanes)

Figure 16 shows the variation of swirl ratio β in the downstream wheel-space against flow coefficient. The swirl was measured in the rotating core at z/S = ¼ and r/b = 0.993 with and without the stator vanes. The data was collected for two purge flow rates, both at the lower rotational speed (Re_ϕ = 7.6×10^5).

The annulus swirl ratio, β_a, downstream of the blades decreases linearly from 0.17 to -0.60 across the range of flow coefficients tested (C_F = 0.26 to C_F = 0.5).

At flow coefficients C_F > 0.31, the mainstream flow in the annulus leaves the rotor blades with negative swirl; across the seal the rotation of the fluid changes direction. Without the vanes, the swirl in the wheel-space reduces monotonically with C_F in a similar manner to the effectiveness in Figure 13. Generally, the vanes reduce the wheel-space swirl with a marked effect over a range of C_F consistent with Figure 13; here fluid with negative swirl enters the outer cavity, demonstrating a clear link between ingestion and swirl. For increased purge momentum (*i.e.* larger Φ_0) the minima in swirl occurs at larger C_F, again suggesting an impact of the egress on the mainstream flow conditions.
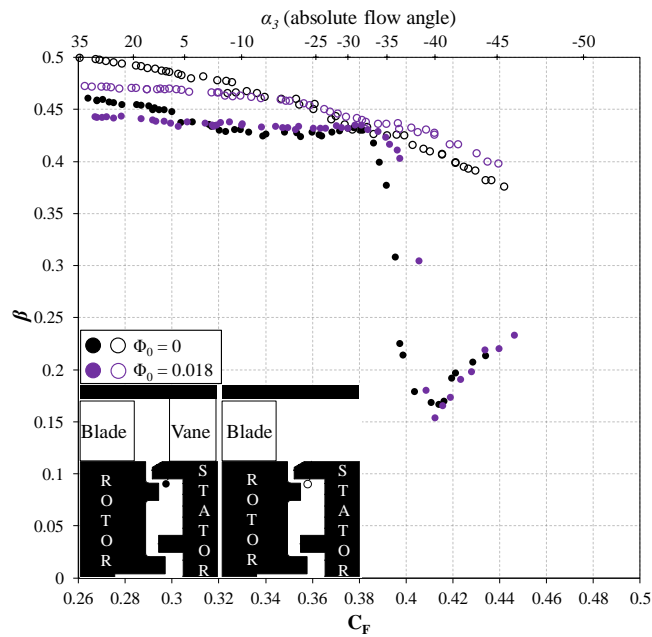
Figure 16: Variation of swirl ratio β with flow coefficient C_F at $r/b = 0.993$. (Solid symbols: Platform with vanes), (Open symbols: Platform without vanes), $\mathrm{Re}_\phi = 7.6\times10^5$

Figure 17 (a) shows the variation of effectiveness and non-dimensional pressure $C_{p,a}$ on the downstream vane platform in the annulus. The data was collected over two vane pitches, with and without vanes; the two pitches $0 < \theta < 1$ and $1 < \theta < 2$ were separated by 180° in the rig and the consistency demonstrates the uniformity of the annulus flow. A silhouette showing the measurement location is provided.

The downstream vanes cause a circumferential variation of pressure and effectiveness and without the vanes this variation is minimal. Effectiveness and pressure for $\Phi_0 = 0.034$ are shown in Figure 17 (a). The trough in the pressure is aligned with the suction surface of the vane and corresponds to a region where the effectiveness is greatest. In the vane passage, away from the stagnation line, the flow velocity is highest and the mixing of mainstream flow with the egress reduces the effectiveness.

Figure 17 (b) shows that the trough in $C_{p,a}$ is seen to displace circumferentially with Φ_0 in the direction of rotation of the blades. This is further evidence that egress from the rim seal acts to locally modify the swirl in the annulus, resulting in increased ingestion when the downstream vanes are present. For the higher sealing flow rates, the non-dimensional difference in pressure distribution $\Delta C_{p,a}$ also becomes larger.

These trends are expected to be replicated on the upstream side in the rotating reference frame upstream of the blade leading edge.


(a)
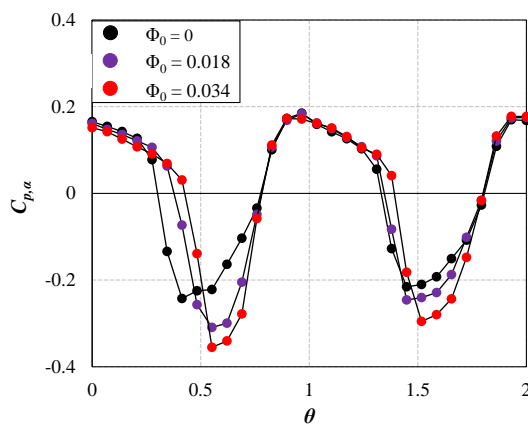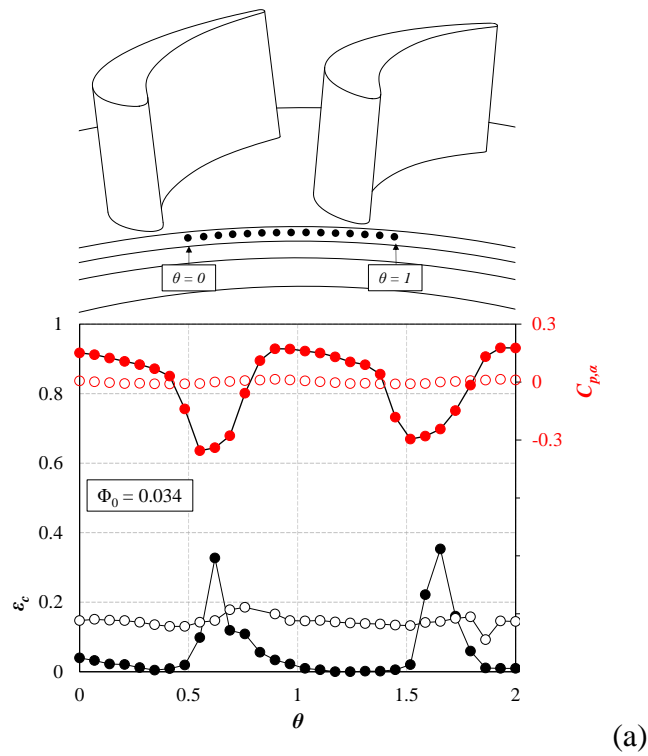
Figure 17: (a) Variation of pressure (red data) and effectiveness (black data) over a vane pitch for $\Phi_0 = 0.034$ (Open symbols: Platform without vanes), (Solid symbols: Platform with vanes), (b) Effect of the purge flow rate on $C_{p,a}$ ($C_F = 0.407$)

4.3 Unsteady Pressure Measurements

Unsteady pressure was measured on the stator upstream of the rotor to interrogate pressure instabilities and large-scale structures in the rim seal gap. As discussed in Section 3.3, two sensors separated by 8° in the azimuthal direction were used inside the outer cavity at $r/b = 0.993$. Data were sampled at 100 kHz over 10 s, with the signals divided into single revolutions of the disc filtered to remove frequencies over the BPF. Cross-correlation of the two signals for every revolution was implemented to determine the lag time. A histogram was used to evaluate the average lag time (Δt_α), rotational speed ($\omega = \alpha / \Delta t_\alpha$) and the number of the structures ($N = (f / f_d)/(\omega / \Omega)$), where f/f_d is the normalised frequency of the rotating structures. Two flow coefficients ($C_F = 0.35$, 0.407) and four sealing flow rates ($\Phi_0 = 0$, 0.018, 0.034, 0.056) were tested with and without the rotor blades at the lower rotational number $Re_\phi = 7.6 \times 10^5$. Although not shown here, the non-dimensional pressure was independent of Re_ϕ.
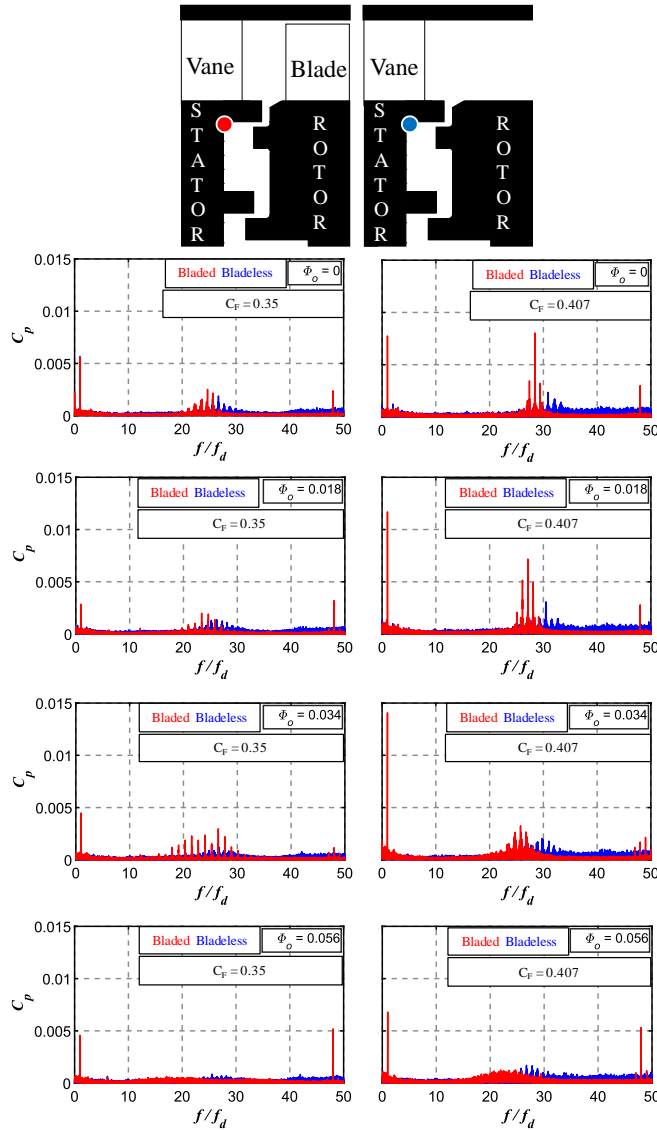
Figure 18: Fast Fourier Transforms of unsteady data measured on the stator wall of the upstream wheel-space at *r/b* = 0.993, with and without the rotor blades. (Re$_\phi$ = 7.6 × 10^5)

Figure 18 shows the FFTs for the unsteady data collected for frequencies up to the normalised BPF *f/f$_d$* = 48, where a distinct peak is observed for the bladed rotor; as expected, no activity is shown for that frequency when the blades are removed. For all plots the main region of interest ranges from 20 < *f/f$_d$* < 30. Increasing the sealing flow

rate generally suppresses the unsteadiness in both configurations. The relative magnitude of C_p for the case with the blades is larger.

The rotational speed of the structures ranged between $0.8 < \omega/\Omega < 1.2$ (note that $\omega/\Omega > 1$ is possible given $\beta_a = 1.6$ for $C_F = 0.407$). Figure 19 shows this rotational speed reduces monotonically with Φ_0 for both the bladed and bladeless rotor. For the same sealing flow rate, ω/Ω increases with C_F. Removing the blades, reduces the speed of the structures. The data shows $19 < N < 28$ with the blades and $27 < N < 32$ for the case without the blades.
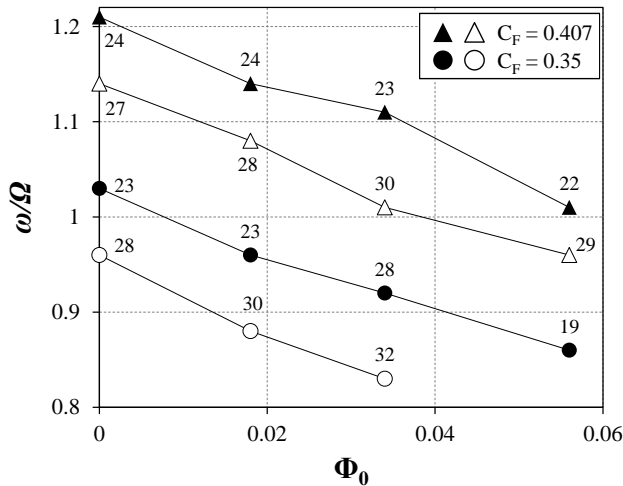
Figure 19: Speed of the large scale structures against Φ_0, numbers next to symbols indicates N, number of structures (Open symbols: Bladeless), (Solid Symbols: Bladed)

5 CONCLUSIONS

The University of Bath 1.5-stage rig was used to measure ingress through rim seals upstream and downstream of the rotor disc. For the upstream wheel-space, two rotors were used: one with blades and one without. For the downstream cavity, the same approach was adopted using a stator platform with vanes and cylindrical ring without.

A double-radial clearance seal was tested in both cavities. Variations of both annulus flow coefficient and non-dimensional sealing flow rate were considered.

Upstream wheel-space. Generally, the blades increase ingress (and ingested swirl) with a marked effect over a relatively narrow range of flow coefficient corresponding to a sweep of relative flow angle equivalent to a downstream blade passage. The ingress is influenced by the interaction between the emergent flow from the rim seal and the rotor blades. *Downstream wheel-space.* Similar trends were observed with the vanes increasing ingress with a ingestion of negative swirl. Measurements on the downstream stator platform showed a clear link between pressure and effectiveness. The non-dimensional vane pressure variation revealed the emergent egress influences the local flow coefficient near the hub leading to increased ingestion.

Unsteady pressure measurements in the upstream wheel-space captured large-scale pressure structures of which the number N and speed ω/Ω depends on the flow coefficient and the purge flow rate. It is hypothesised that the low pressure caused by these structures draws fluid in from the annulus reducing the effectiveness inside the wheel-space. Without the rotor blades, the structures were still present, however the blade-vane interaction influenced their intensity and modified the frequency at which they occur.

NOMENCLATURE

A_p amplitude of unsteady pressure (*Pa*)

b radius of seal (*m*)

c concentration of tracer gas

C absolute velocity (*m/s*)

C_F flow coefficient (*W/Ωb*)

C_p pressure coefficient $(= A_p / \tfrac{1}{2}\rho\Omega^2 b^2)$

$C_{p,a}$ pressure coefficient in annulus $(= (p_a - \bar{p}_a)/\tfrac{1}{2}\rho\Omega^2 b^2)$

f measured frequency (Hz)

fd frequency of disk rotations (Hz)

G_c seal-clearance ratio $(= s_{c,ax}/b)$

h height of annulus (m) and enthalpy (J/kg)

$\dot{m}$ mass flow rate (kg/s)

M Mach number

N Number of large-scale structures around disc

p static pressure (Pa)

p_{baro} barometric (atmospheric) pressure (Pa)

p_T total pressure (Pa)

r radius (m)

Re_w axial Reynolds number in annulus based on radius $(= \rho W b/\mu)$

Re_ϕ rotational Reynolds number $(= \rho\Omega b^2/\mu)$

s_c seal clearance (m)

S axial clearance between rotor and stator (m)

U bulk mean radial seal velocity $(= \dot{m}_0/2\pi\rho b s_c)$

V_ϕ tangential velocity (m/s)

V velocity relative to blades (m/s)

W axial velocity in annulus (m/s)

z axial coordinate (m)

α angle between unsteady pressure transducers (rad)

α_2 absolute upstream vane exit angle (deg)

α_3 absolute downstream vane inlet angle (deg)

β swirl ratio $(= V_\phi/(\Omega r))$

β_2 relative blade inlet angle (*deg*)

β_3 relative blade exit angle (*deg*)

$\Delta C_{p,a}$ pressure coefficient in annulus $(= \Delta p_a / \frac{1}{2}\rho\Omega^2 b^2)$

Δp_a peak-to-trough pressure difference in annulus $(= p_{a,max} - p_{a,min})$

Δt_α time for large scale structure to move through

     angle α (s)

ε_c concentration effectiveness

θ non-dimensional vane pitch

μ dynamic viscosity (*kg/ms*)

ρ density (*kg/m³*)

Φ_0 non-dimensional sealing parameter $(= U/\Omega b)$

Ω angular speed of rotating disc (*rad/s*)

ω angular speed of large scale structures (*rad/s*)

Subscripts

a   annulus

ax   axial

m   midspan

rad   radial

0   sealing flow

2   location upstream of blades

3   location downstream of blades

Appendix: Uncertainty Analysis

The uncertainty analysis provides a methodical approach to evaluate the quality of any presented results. **Table A.1** and **Table A.2** present the measurement uncertainty for the upstream and downstream wheel-space respectively.

Dimension	Uncertainty
$\delta C_F/C_F$	1.1%
$\delta \Phi_0/\Phi_0$	2%
$\delta \varepsilon_c/\varepsilon_c$	1.8%
$\delta \beta/\beta$	1.2%

Table A.1: Estimated measurement uncertainty.   Upstream wheel-space, $\Phi_0 = 0.056$, $C_F = 0.35$

Dimension	Uncertainty
$\delta C_F/C_F$	1.1%
$\delta \Phi_0/\Phi_0$	3.5%
$\delta \varepsilon_c/\varepsilon_c$	1.4%

Table A.2: Estimated measurement uncertainty. Downstream wheel-space, $\Phi_0 = 0.034$, $C_F = 0.35$

X_i	δX_i	Range
$c_s,\ c_a,\ c_0$	$\pm 1\%$ FS	$0 - 1\%$ CO_2

$\dot{m}_0$	±1% FS	0 – 0.048 kg/s
$\dot{m}_{an}$	±1% of reading	0 – 1.7 kg/s
p_{baro}	±1% mbar	954 – 1073 mbar
p_{an}	±0.3% FS	0 – 150 mbar
p_{ws}, p_s, p_t, p_a	±0.3% FS	0 – 80 mbar
T	±0.5 K	283 – 303 K
Ω	±1 rpm	0 – 5000 rpm

Table A.3: Instrumentation accuracy

As an example of the analysis, the uncertainty calculation for the flow coefficient C_F is shown.
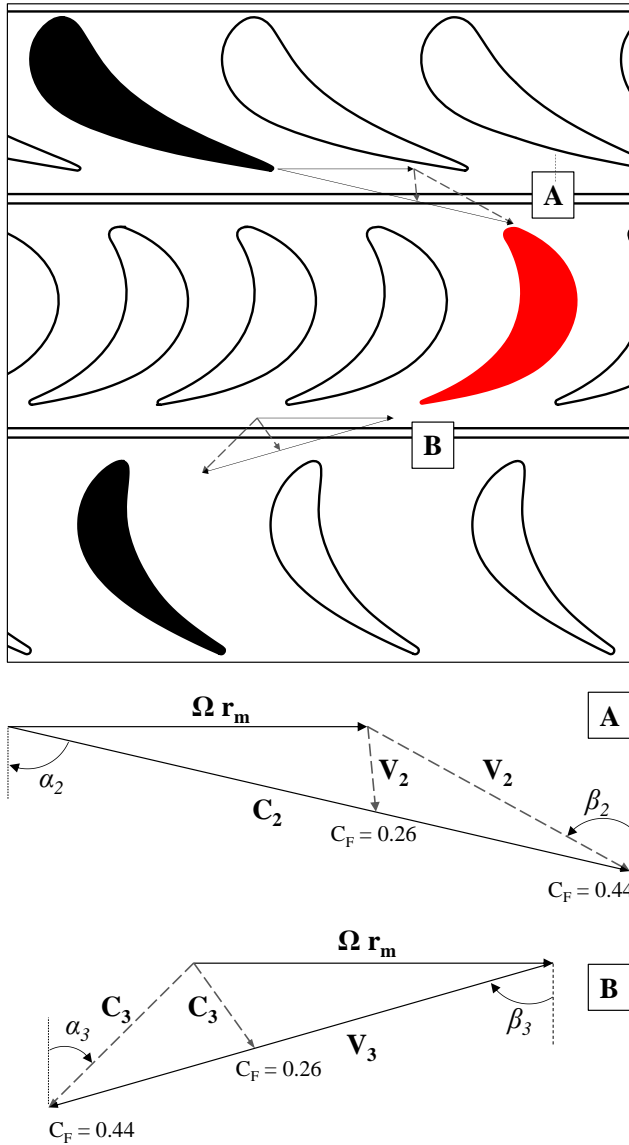
The flow coefficient is defined as:

$$C_F = \frac{\dot{m}_{an}\, R\, T}{(p_{baro} + p_{an})\, \pi\, (r_{shroud}^2 - r_{hub}^2)\, \Omega\, b}$$

Ignoring any geometric uncertainties:

$$\left(\frac{\delta C_F}{C_F}\right)^2 = \left(\frac{\delta \dot{m}_a}{\dot{m}_a}\right)^2 + \left(\frac{\delta T}{T}\right)^2 + \left(\frac{\delta \Omega}{\Omega}\right)^2 + \frac{\delta p_{baro}^2 + \delta p_{an}^2}{(p_{baro} + p_{an})^2}$$

Repeating the above analysis for all the other quantities, Tables A.1 and A.2 are calculated.

Appendix: Velocity Triangles

Figure 20: Velocity triangles shown upstream and downstream of the blade for the range of flow coefficients tested

References

[1] Cumpsty, N.A. 2010, "Preparing for the Future: Reducing Gas Turbine Environmental Impact – IGTI Scholar Lecture," ASME J. Turbomach., **132**(132), 041017-1.

[2] Scobie, J. A., Sangan, C. M., Owen, J. M., and Lock, G. D., 2016, "Review of Ingress in Gas Turbines," ASME J. Eng. Gas Turbines Power, **138**(12), p. 120801.

[3] Chew, J. W., Gao, F., and Palermo, D. M., 2019, "Flow Mechanisms in Axial Turbine Rim Sealing," Proc. Inst. Mech. Eng. Part C J. Mech. Eng. Sci., **233**(23–24), pp. 7637–7657.

[4] Revert, A. B., Beard, P. F., Chew, J. W., and Bottenheim, S., 2020, "Performance of a Turbine Rim Seal Subject to Rotationally-Driven and Pressure-Driven Ingestion," ASME Paper No. GT2020-14773

[5] Hualca, F. P. T., Horwood, J. T. M., Sangan, C. M., Lock, G. D., and Scobie, J. A., 2019, "The Effect of Vanes and Blades on Ingress in Gas Turbines." ASME J. Eng. Gas Turbines Power, **142**(2), p. 021020.

[6] Beard, P. F., Gao, F., Chana, K. S., and Chew, J., 2017, "Unsteady Flow Phenomena in Turbine Rim Seals," J. Eng. Gas Turbines Power, **139**(3), p. 032501.

[7] Savov, S. S., Atkins, N. R., and Uchida, S., 2017, "A Comparison of Single and Double Lip Rim Seal Geometries," ASME J. Eng. Gas Turbines Power, **139**(11), p. 112601.

[8] Horwood, J. T. M., Hualca, F. P., Wilson, M., Scobie, J. A., Sangan, C. M., Lock, G. D., Dahlqvist, J., and Fridh, J., 2020, "Flow Instabilities in Gas Turbine Chute Seals," J. Eng. Gas Turbines Power, **142**(2), p. 021019.

[9] Gao, F., Chew, J. W., and Marxen, O., 2020, "Inertial Waves in Turbine Rim Seal Flows," Physical Review Fluids, **5**, 024802.

[10] Gallier, K. D., Lawless, P. B., and Fleeter, S., 2004, "Development of the Unsteady Flow on a Turbine Rotor Platform Downstream of a Rim Seal," ASME Paper No. GT2004-53899.

[11] Schädler, R, Kalfas, A.I., Abhari, R.S., Schmid, G. and Voelker, S., 2016, Modulation and radial migration of turbine hub cavity modes by the rim seal purge flow, ASME GT2016-56661.

[12] Patinios, M., Scobie, J. A., Sangan, C. M., Owen, J. M., and Lock, G. D., 2017, "Measurements and Modeling of Ingress in a New 1.5-Stage Turbine Research Facility," J. Eng. Gas Turbines Power, **139**(1), p. 012603.

[13] Patinios, M., Scobie, J. A., Sangan, C. M., and Lock, G. D., 2017, "Performance of Rim-Seals in Upstream and Downstream Cavities over a Range of Flow Coefficients," Int. J. Turbomach. Propuls. Power, 2(4), 21.